Figure S1

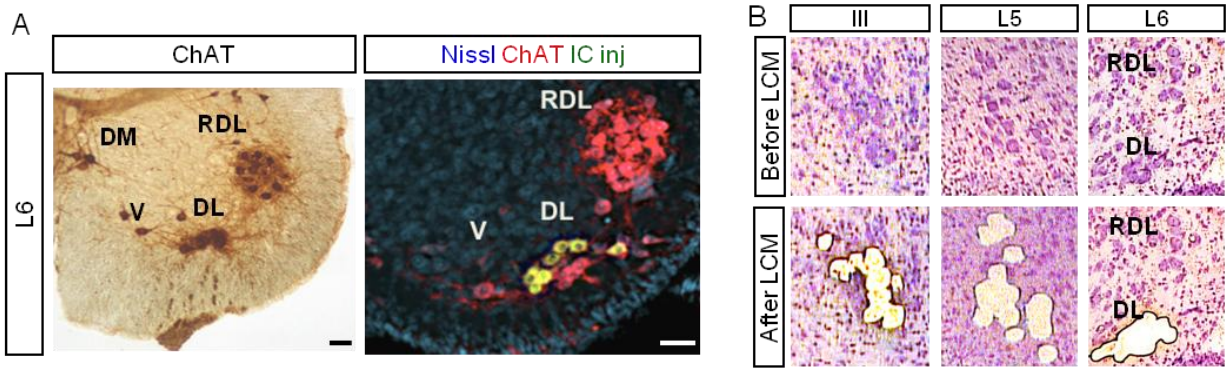

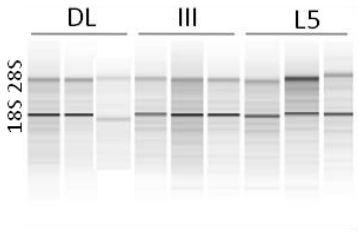

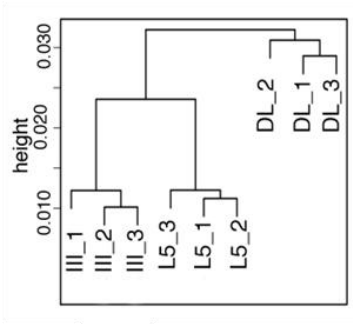

E

Probeset ID	Gene Symbol	Fold Δ DL / L5	Fold Δ III / L5
1455907_x_at	*Phox2b*	n.s.	44
1453351_at	*Tbx20*	n.s.	39
1417653_at	*Pvalb*	n.s.	12
1431475_a_at	*Hoxa10*	n.s.	-64
1439798_at	*Hoxc10*	n.s.	-549
1460299_at	*Mnx1*	n.s.	-8
1450177_at	*Ngfr*	15	ns
1417504_at	*Calb1*	5	-2

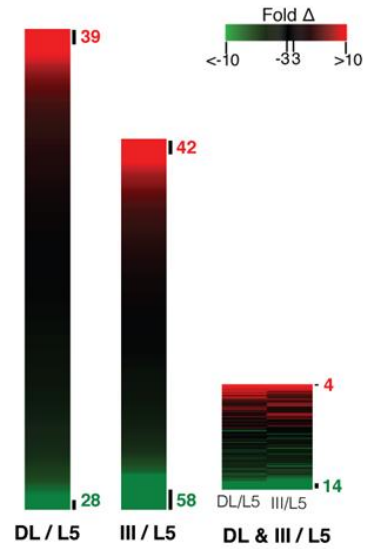

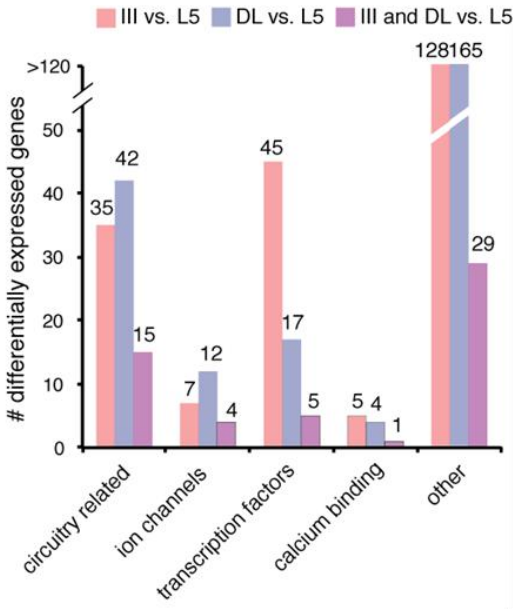

Table S1

			Fold Δ			
Probeset ID	Gene full name	Gene symbol	DL / L5	III / L5	Function/ category	Reference
1421978_at	glutamic acid decarboxylase 2	*Gad2*	16.4	10.1	neurotransmitter biosynthesis	Esclapez et al., 1994
1442226_at	semaphorin 3E	*Sema3e* *	68.9	58.1	axon guidance	Chauvet et al., 2007
1441590_at	potassium inwardly-rectifying channel, subfamily J, member 5	*Kcnj5*	15.8	17.0	ion channel	Bettahi et al., 2002
1424763_at	RIKEN cDNA 1700027N10 gene	*1700027N10Rik*	12.8	10.9	Rsph9, radial spoke head 9 homolog (Chlamydomonas), cilium axoneme assembly	Castleman et al., 2009
1421391_at	vasoactive intestinal peptide receptor 2	*Vipr2*	-11.4	-14.5	neuromodulator receptor, G protein-coupled receptor	Harmar et al., 2002
1449572_at	thyrotropin releasing hormone receptor	*Trhr* *	-18.0	-72.7	neuromodulator receptor, G protein-coupled receptor	Gershengorn et al., 1996
1450286_at	natriuretic peptide receptor 3	*Npr3* *	-11.1	-12.5	neuromodulator receptor, G protein-coupled receptor	Potter et al., 2006
1422860_at	neurotensin	*Nts* *	-120.1	-19.2	peptide neurotransmitter	Mai et al., 1987
1449031_at	Cbp/p300-interacting transactivator with Glu/Asp-rich carboxy-terminal domain 1	*Cited1*	-20.0	-15.2	transcription regulation	Dunwoodie et al., 1998
1449939_s_at	delta-like 1 homolog (Drosophila)	*Dlk1*	-15.6	-14.6	atypical Notch ligand	Ferron et al., 2011
1422789_at	aldehyde dehydrogenase family 1, subfamily A2	*Aldh1a2*	-19.4	-274.7	retinoic acid biosynthesis, developmental signaling	Sockanathan and Jessell, 1998
1425958_at	interleukin 1 family, member 9	*Il1f9*	-17.7	-18.7	secreted protein, cytokine activity	Vigne et al., 2011
1418352_at	hydroxysteroid (17-beta) dehydrogenase 2	*Hsd17b2* *	-35.5	-32.9	androgen biosynthesis	Penning et al., 1997
1418649_at	EGL nine homolog 3 (C. elegans)	*Egln3* *	-13.2	-11.9	hypoxia response, pro-apoptotic	Fong and Takeda, 2008
1456777_at	maltase-glucoamylase	*Mgam*	-13.2	-13.7	disaccharide digestion, cell metabolism	Quezada-Calvillo, 1993
1448291_at	matrix metallopeptidase 9	*Mmp9* *	-16.0	-11.1	extracellular matrix remodelling, synaptic plasticity	Visse et al., 2003
1424249_a_at	Rho GTPase activating protein 9	*Arhgap9*	-13.9	-22.0	signal transduction	Furukawa et al., 2001
1423261_at	RIKEN cDNA 1500015O10 gene	*1500015O10Rik*	-11.8	-23.8	aka augurin, Ecrg4, secreted protein, developmental regulation, senescence induction	Kujuro et al., 2010

Figure S2

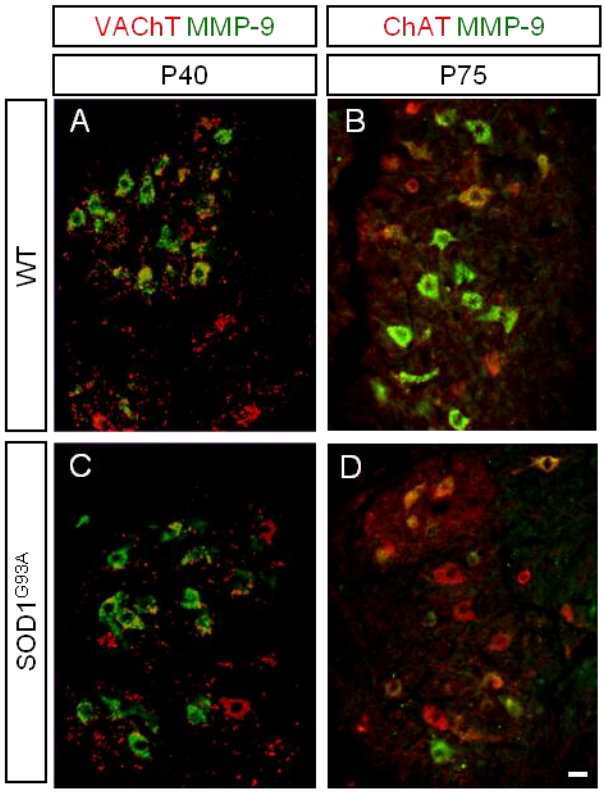
VAChT MMP-9
ChAT MMP-9
P40
P75
A
B
C
D
WT
SOD1G93A

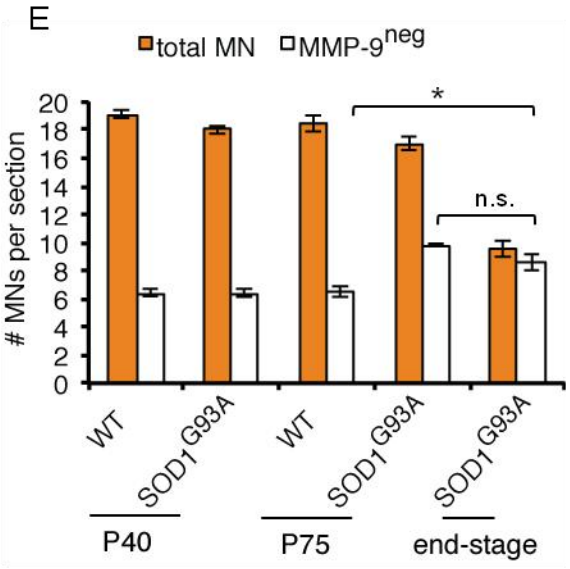
E
total MN
MMP-9neg
MNs per section
20
18
16
14
12
10
8
6
4
2
0
*
n.s.
WT
SOD1G93A
WT
SOD1G93A
SOD1G93A
P40
P75
end-stage

Figure S3

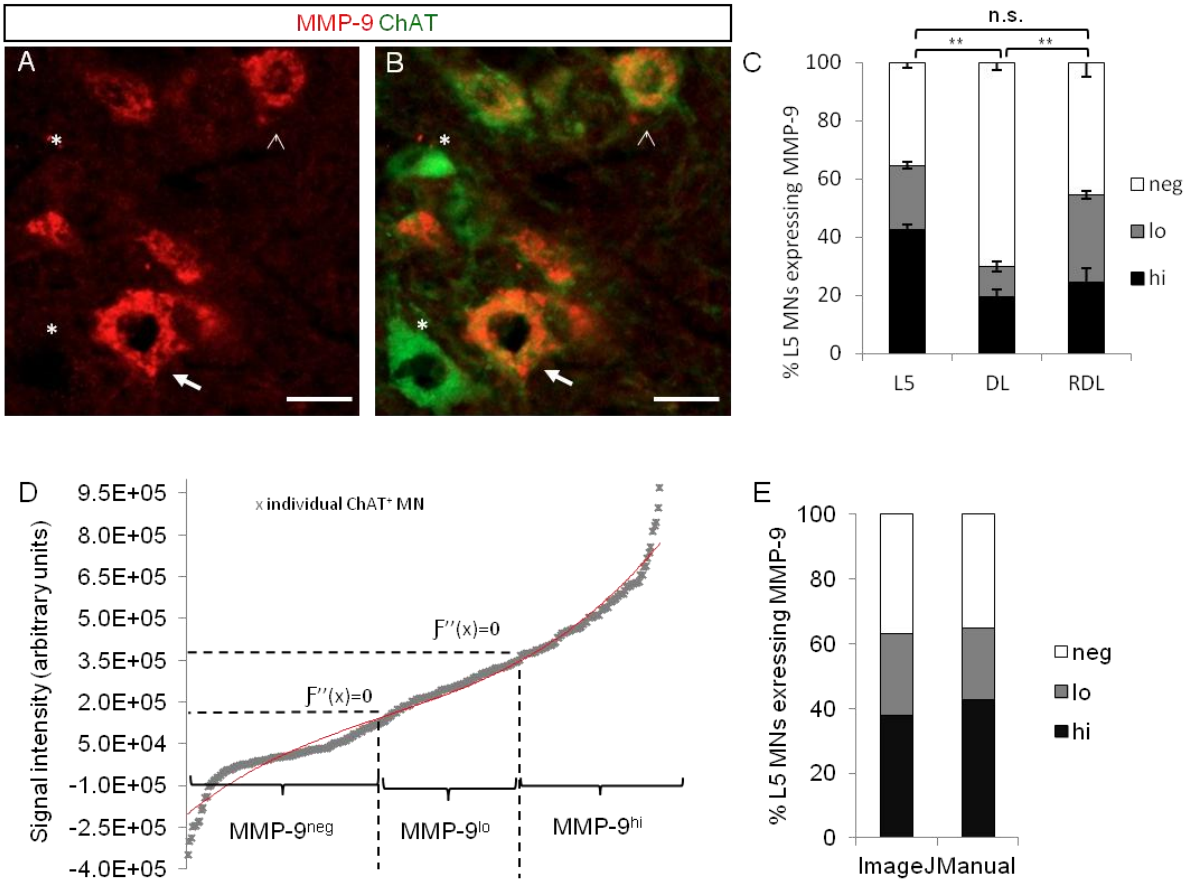
MMP-9 ChAT
A
B
C
n.s.
**
**
100
80
60
40
20
0
% L5 MNs expressing MMP-9
L5
DL
RDL
neg
lo
hi
D
9.5E+05
8.0E+05
6.5E+05
5.0E+05
3.5E+05
2.0E+05
5.0E+04
-1.0E+05
-2.5E+05
-4.0E+05
Signal intensity (arbitrary units)
x individual ChAT+ MN
F''(x)=0
F''(x)=0
MMP-9neg
MMP-9lo
MMP-9hi
E
100
80
60
40
20
0
% L5 MNs exressing MMP-9
ImageJ
Manual
neg
lo
hi

Figure S4

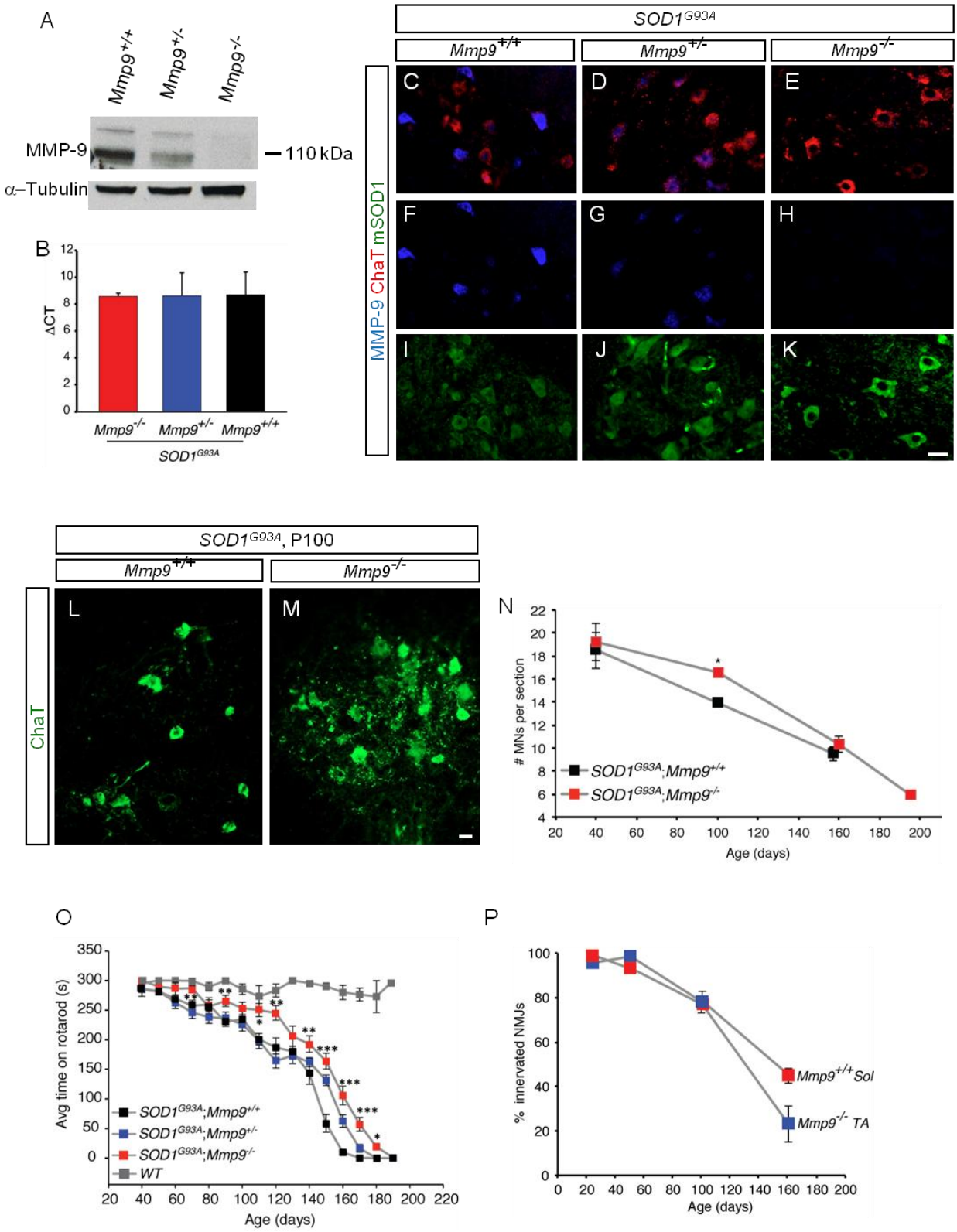
A
Mmp9+/+
Mmp9+/-
Mmp9-/-
MMP-9
110 kDa
α–Tubulin
B
ΔCT
Mmp9-/-
Mmp9+/-
Mmp9+/+
SOD1G93A
SOD1G93A
Mmp9+/+
Mmp9+/-
Mmp9-/-
MMP-9 ChaT mSOD1
C
D
E
F
G
H
I
J
K
SOD1G93A, P100
Mmp9+/+
Mmp9-/-
ChaT
L
M
N
MNs per section
SOD1G93A;Mmp9+/+
SOD1G93A;Mmp9-/-
Age (days)
O
Avg time on rotarod (s)
SOD1G93A;Mmp9+/+
SOD1G93A;Mmp9+/-
SOD1G93A;Mmp9-/-
WT
Age (days)
P
% innervated NMJs
Mmp9+/+ Sol
Mmp9-/- TA
Age (days)

Figure S5

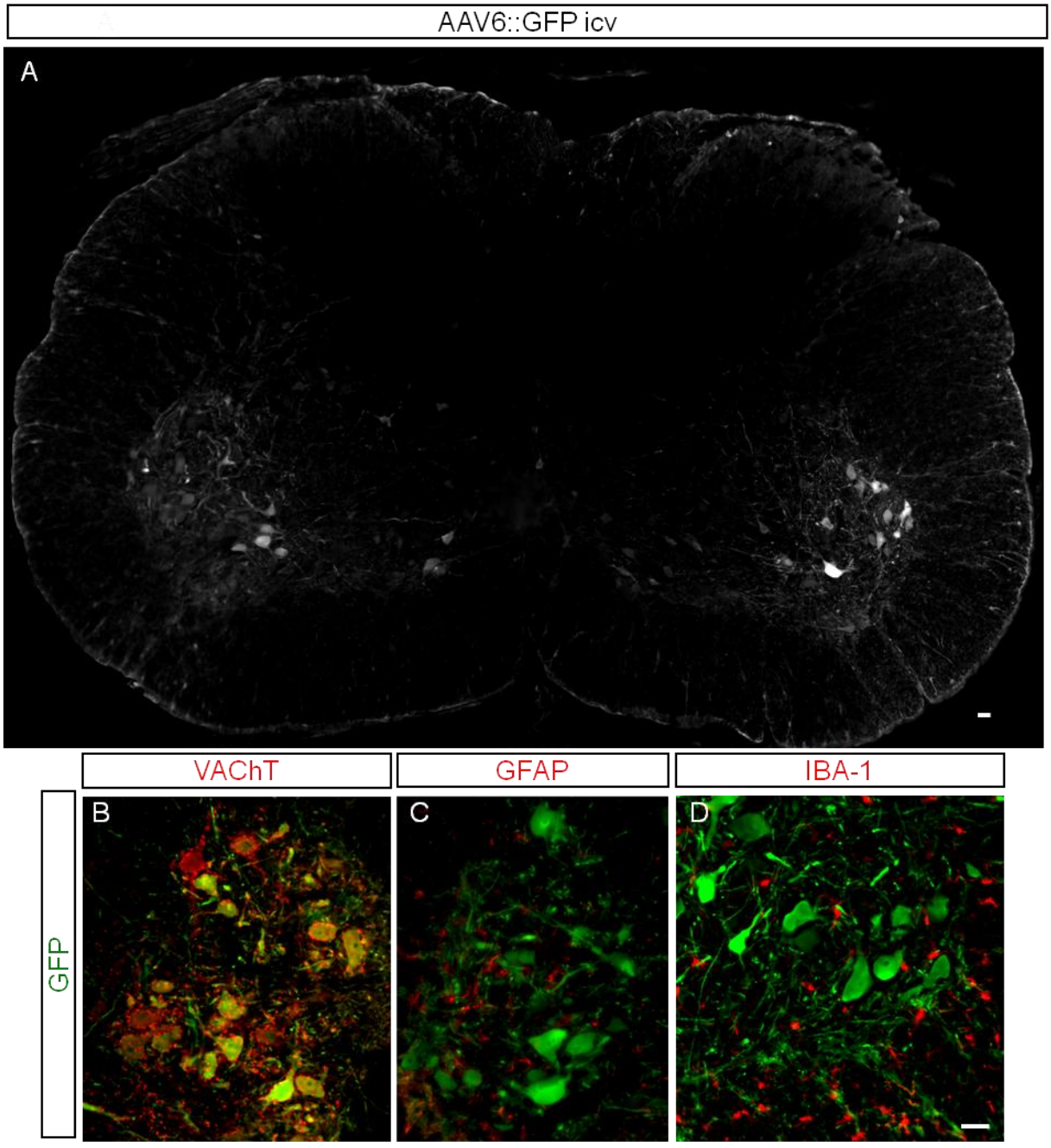

Figure S6

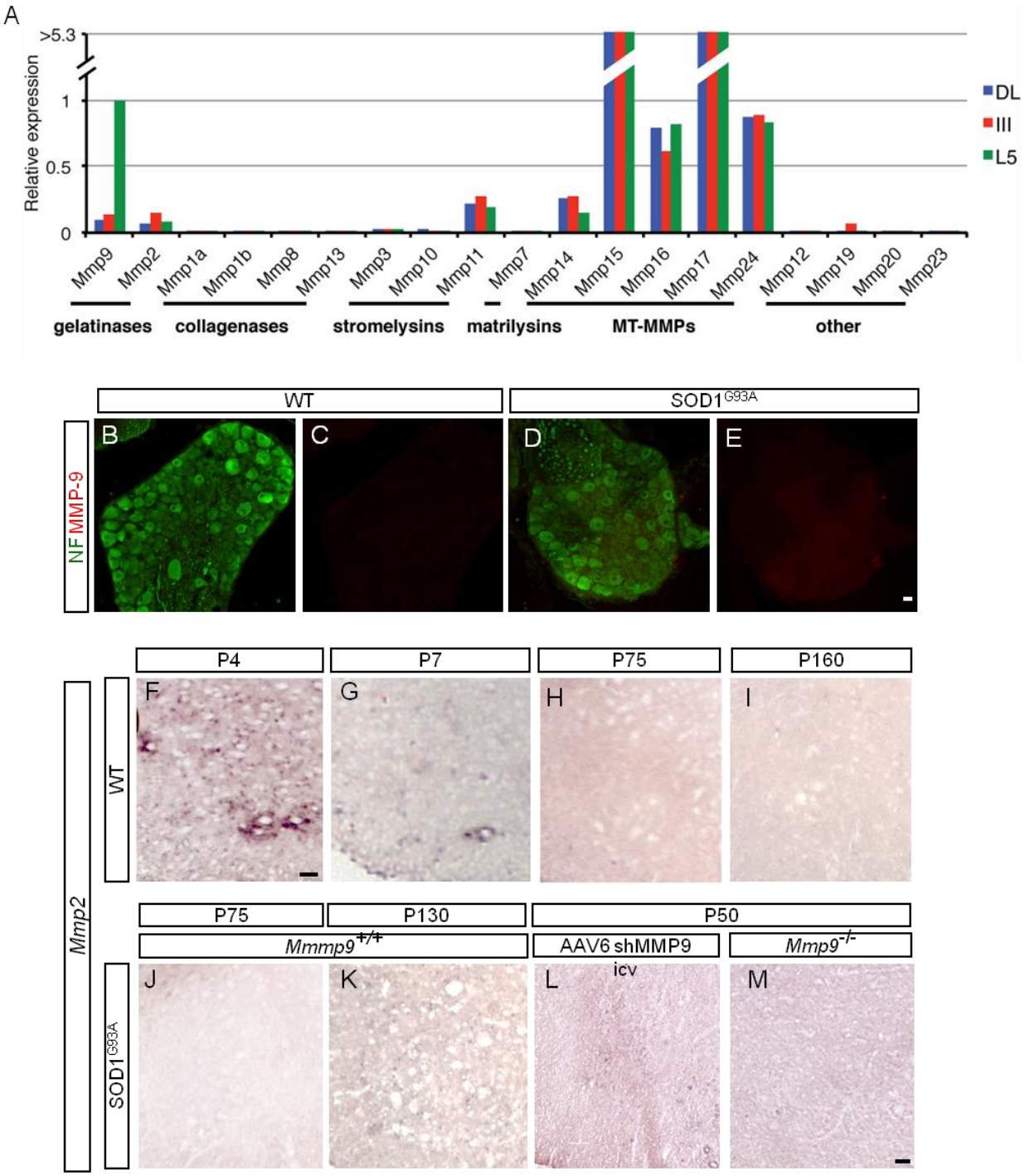
A
>5.3
1
0.5
0
Relative expression
DL
III
L5
Mmp9
Mmp2
Mmp1a
Mmp1b
Mmp8
Mmp13
Mmp3
Mmp10
Mmp11
Mmp7
Mmp14
Mmp15
Mmp16
Mmp17
Mmp24
Mmp12
Mmp19
Mmp20
Mmp23
gelatinases
collagenases
stromelysins
matrilysins
MT-MMPs
other
WT
SOD1G93A
NF MMP-9
B
C
D
E
P4
P7
P75
P160
Mmp2
WT
F
G
H
I
P75
P130
P50
Mmmp9+/+
AAV6 shMMP9
icv
Mmp9-/-
SOD1G93A
J
K
L
M

Supplemental Figure Legends

Figure S1. Laser capture and microarray analysis of identified postnatal motor neuron populations, Related to Figure 1.

(A) Localization of motor pools composing the mouse Onuf's nucleus at the L6 level of the spinal cord. Left: choline acetyltransferase (ChAT) immunostaining reveals ventral (V), dorsolateral (DL), dorsomedial (DM) and retrodorsolateral (RDL) pools. Right: the identity of the DL nucleus confirmed by CTB-488 injection into the IC muscle at P7. Scale bar, 20 µm.

(B) Laser capture microdissection (LCM) of vulnerable and resistant motor neurons**.** Cresyl violet-stained cryosections before and after capture of the oculomotor nucleus (III), L5 motor neurons, and DL nucleus.

(C) Quality of RNA from the LCM of motor neurons from III, DL, and L5 as assessed by Bioanalyzer. Three biological replicates are shown for each nucleus. Note intact 28S and 18S rRNA bands in all samples.

(D) Clustering analysis using Pearson correlation as matrix and average distance on all genes present on the arrays shows clustering of the individual replicates into three groups (III, L5, and DL) corresponding to the three samples of each motor neuron population.

(E) Validation of the microarray data by examples of genes already known to be expressed specifically in oculomotor or cranial motor neurons (*Phox2b*, *Tbx20*, *Pvalb*), in the DL nucleus (*Ngfr*, *Calb1*), or in L5 motor neurons (*Hoxa10*, *Hoxc10*). *Mnx1 (Hb9)* is expressed by spinal (DL and L5) motor neurons but is absent as expected from cranial (III) motor neurons.

(F) Heat map representation of all >3-fold gene expression differences between indicated population. Each gene is indicated as a single line, sorted by fold-change values from most enriched versus L5 (bright red) to most depleted (bright green). To identify genes regulated in common in both resistant populations versus L5, each gene was assigned a distance from point 0 representing no differential expression. Distance was calculated as the absolute value of the lower of the two fold-change values between DL and III.

(G) Gene ontology assignation for > 5-fold differences between the indicated motor neuron populations. Circuitry-related combines: synaptic proteins, neurotransmitters, neurotransmitter receptors, axon guidance factors. Note that majority of differentially expressed genes did not fit into any of these categories.

Table S1. Functional annotations for 18 most regulated genes, Related to Figure 1. Annotations were derived from PubMed and MGI**.** *validated by *in situ* hybridization.

Figure S2. The pattern of MMP-9 expression is not altered in motor neurons of presymptomatic mSOD1 mice, but is down-regulated by some neurons late in the disease process, Related to Figure 2.

(A, C and E) L5 spinal cord of $SOD1^{G93A}$ and age-matched WT control mice at P40 immunostained for MMP-9 (green) and VAChT (red) shows that the presence of mutant SOD1 does not affect MMP-9 expression.

(B, D and E) At P75, there is no reduction in total motor neuron numbers (unpaired Student's t-test, p=0.14) but the number of MMP-9-negative motor neurons increased by 50% (unpaired Student's t-test, p=0.0007), suggesting that some motor neurons lose MMP-9 expression. By end-stage, although there is a 50% loss of total motor neurons, there is no decrease in the number of $MMP\text{-}9^{neg}$ motor neurons, suggesting that they constitute the ALS-resistant population. Values are mean ± s.e.m from three animals. *, $p<0.05$.

Figure S3. Quantification of MMP-9 immunoreactivity in lumbar motor neurons, Related to Figure 3.

(A) Quantification of MMP-9 staining intensities in L5, DL and RDL motor neurons (mean ± s.e.m, n=3-4). Resistant DL nucleus motor neurons expressed significantly lower levels of MMP-9 than did vulnerable L5 or RDL. A two-way analysis of variance showed that differences between motor neuron subsets were significant [$F(4, 29) = 34.1, p<0.001$]. *Post hoc* comparisons using the Bonferroni analysis revealed that the DL nucleus contained a significantly higher proportion of $MMP\text{-}9^{neg}$ motor neurons than L5 ($t= 9.06$, $p<0.01$) or RDL ($t= 6.00$, $p<0.01$).

(B) Scatter plot of MMP-9 signal corrected for background in a fixed area within each of 273 motor neurons in the L5 spinal cord of one animal. A 3^{rd} order polynomial best fit trend line (red), determined by maximizing the R^2 value (>0.98), was added and the second derivative was taken to find two inflection points of the function. The ordinate values of the two inflection points were set to be the bin thresholds. All motor neurons with MMP-9 intensity lower than the first inflection point were considered $MMP\text{-}9^{neg}$, those between the two inflection points were considered $MMP\text{-}9^{lo}$, while all above were considered $MMP\text{-}9^{hi}$.

(C) Close correspondence between automated and manual counts. Fraction of each category in L5 calculated by automated image analysis in D (ImageJ) or by manual counting in C (Manual).

Figure S4. MMP-9 levels and additional phenotypes in mSOD1 mice crossed to MMP-9 knockouts, Related to Figure 5.

(A) Western blotting reveals that MMP-9 levels in the heterozygote are 44% of the wildtype control. Densitometry values were normalized using α-tubulin.

(B) No changes in SOD1^{G93A} copy number in the absence of MMP-9. Quantitative real-time PCR (qPCR) data using the Delta Ct method are shown.

(C to K) Immunostaining for ChAT (red), MMP-9 (blue), and mSOD1 (green) at P40 in L5 spinal cord of indicated genotypes. Overall motor neuron numbers are similar but MMP-9 intensity per cell reflects the null or heterozygote genotype. Note complete absence of MMP-9 staining in the *SOD1^{G93A};Mmp9$^{-/-}$* spinal cord, demonstrating the specificity of the MMP-9 antibody. No significant difference in intensity of mSOD1 staining was noted between three *Mmp9* genotypes.

(L and M) Motor neurons visualized using ChAT immunostaining at the L5 level of the spinal cord of P100 *SOD1^{G93A};Mmp9$^{+/+-}$* and SOD1^{G93A}*;Mmp9$^{-/-}$* littermates.

(N) Direct counting of motor neurons at L5 from P40 to end-stage shows a significant delay in loss in the absence of MMP-9 (n=3-5; p=0.003 at P100).

(O) Latency to fall from an accelerating rotarod. Animals were tested twice weekly for their ability to stay on an accelerating rotating rod, beginning when they were 40 days old. Testing was discontinued for individuals when they were no longer able to remain on the rotarod for 5 seconds. SOD1^{G93A};*Mmp9$^{-/-}$* mice performed better than controls from P70 onward as assessed by one-way ANOVA at each time-point (***, p<0.001, **, P< 0.01; *, p<0.05). SOD1^{G93A};*Mmp9$^{+/-}$* showed improved performance from P150 (p<0.001).

(P) No significant differences at early time-points between the degree of innervation of the slow soleus muscle of SOD1^{G93A} mice (red points) and the "fast" TA of *SOD1^{G93A};Mmp9$^{-/-}$* mice (blue points).

Movie S1. Deletion of a single or both *Mmp-9* alleles confers significant functional benefit in SOD1^{G93A} mice at P150, Related to Figure 5. Animals shown are male littermates of the indicated genotypes examined at the same time. Whereas the normal SOD1^{G93A} mutant is close to the endpoint for euthanasia, the *Mmp*-9 knockout shows normal grasping and hindlimb position. Although the *Mmp-9* heterozygote has splay defects, minor weight loss, and a visible gait abnormality, it is significantly improved as compared to the SOD1^{G93A} control. Subsequent times to euthanasia for each animal shown were: 0 days (*SOD1^{G93A};Mmp9$^{+/+}$*), 27 days (*SOD1^{G93A};Mmp9$^{+/-}$*) and 53 days (*SOD1^{G93A};Mmp9$^{-/-}$*).

Figure S5. AAV6 delivered i.c.v. selectively infects motor neurons, related to Figure 8.

(A-D) AAV6 delivered i.c.v. selectively infects motor neurons and very few other cell types as shown here by representative immunostained cryosections of adult lumbar cord. GFP staining overlaps with

VAChT-labeled motor neurons (B), but not GFAP-labeled astrocytes (C) or IBA-1 labeled microglia (D). Scale bars, 20 μm.

Figure S6. Expression of other MMP family members in motor neurons, Related to Discussion.
(A) MMP-9 is the only secreted MMP expressed at high levels in motor neurons at P7. Raw expression values for indicated probes on microarrays for DL, III, and L5 samples were divided by the raw expression value of *Mmp9* in L5 motor neurons. Transcripts were arranged into known subgroups based on protein domains and substrate specificity including: gelatinases (*Mmp9* and *Mmp2*), collagenases (*Mmp1a*, *Mmp1b*, *Mmp8*, *Mmp13*), stromelysins (*Mmp3*, *Mmp10*, *Mmp11*), matrilysins (*Mmp7*) and membrane-type (MT–MMPs) (*Mmp14*, *Mmp15*, *Mmp16*, *Mmp17*, *Mmp24*), and other (*Mmp12*, *Mmp19*, *Mmp20*, *Mmp23*). Probes for *Mmp25*, *Mmp26*, and *Mmp28* were not present on the array. Only members of the MT-MMP subgroup showed similar or higher expression levels as compared to *Mmp9* whereas all other MMPs, including *Mmp2*, were nearly absent. *Mmp15* and *Mmp17* had >4-fold higher expression values compared to *Mmp9* but were not specific to L5 motor neurons.
(B to E) No MMP-9 staining (red) was detected in dorsal root ganglion neurons co-labeled for neurofilament (NF, green) from a P30 WT or a P60 $SOD1^{G93A}$ mouse. Scale bar 20 μm.
(F to M) *In situ* hybridization for *Mmp2* on cryosections of L5 spinal cord at indicated ages and genotypes. In WT mice, MMP-2, the other member of the gelatinase family, is expressed by few motor neurons at P4 and P7 (F,G) but is absent from motor neurons at later ages (H,I). MMP-2 expression is not upregulated in $SOD1^{G93A}$ mice (J-K) and does not compensate for viral-mediated silencing (L) or genetic deletion (M) of *Mmp9*.

Supplemental Experimental Procedures

Transgenic Mice

For expression studies, ChAT-Cre [B6;129S6-Chattm1(cre)Lowl/J] and Rosa-TdTomato reporter [B6;129S6-Gt(ROSA)26Sortm14(CAG-tdTomato)Hze/J] mice were purchased from the Jackson Laboratory (Bar Harbor, ME) and crossed so that, after the CRE recombination, the resultant offspring's motor neurons are marked by the expression of TdTomato. *Chodl-LacZ* mice were obtained from Lexicon Pharmaceuticals.

Mice heterozygous for the mutant human $SOD1^{G93A}$ transgene (B6.Cg-Tg(SOD1*G93A)1Gur/J Jackson Laboratory) were crossed with mice heterozygous for an MMP9 gene disruption (B6.FVB(Cg)-

Mmp9^{tm1Tvu}/J, Jackson Laboratory), both on a C57BL/6J background. For all experiments, *SOD1*^{G93A}*; Mmp9*$^{-/-}$ mice were always compared with their contemporaneously produced *SOD1*^{G93A}*; Mmp9*$^{+/+}$ or *SOD1*^{G93A}*; Mmp9*$^{+/-}$ littermates. The clinical course for the mutant SOD1 mice was monitored weekly. The disease invariably progressed from hindlimb tremor, and reduced splay to gait abnormalities, followed by complete paralysis. End-stage of disease was defined as the age at which mutant SOD1 mice could no longer right themselves for 30 seconds after being put on their side. All animal work was performed in compliance with the Columbia University IACUC protocols.

Microarray

For the Affymetrix gene chip array study, three wild-type C57BL/6J P7 male animals were perfused with 30% sucrose, lumbosacral spinal cord and midbrain regions were rapidly recovered, embedded in OCT compound, and frozen in liquid nitrogen. 12 µm-thick cryosections were mounted on RNAse-free, PEN-foil covered glass slides (Zeiss), fixed for 2 min in 100% EtOH, rinsed in 50% EtOH, stained with 1% cresyl violet for 2 min, rinsed with 50% EtOH, dehydrated in graded solutions of ethanol and air dried prior to LCM using PALM Microbeam system (Zeiss). From each animal, ~200 DL, L5, and oculomotor motor neurons were collected directly in lysis buffer. RNA was purified using Absolutely RNA, NanoPrep kit (Stratagene, La Jolla, CA). RNA integrity was assessed on the Bioanalyzer 2100 (Agilent Technologies, Santa Clara, CA). At least 1.5 ng of purified RNA was the starting material used in the WT-Ovation Pico RNA Amplification System (Nugen, San Carlos,CA) with the FL-Ovation cDNA Biotin Module V2 (Nugen) to generate labeled probe. 10 µg of biotinylated cRNA from three independent samples for each motor neuron group isolated by LCM was hybridized to on Affymetrix (Santa Clara, CA) Mouse Genome 430 2.0 Arrays. Gene ontology and pathway analysis was performed using DAVID Bioinformatics Resources 6.7 (National Institute of Allergy and Infectious Diseases, NIH, Bethesda, MD).

Immunohistochemistry

Mice were deeply anesthetized using avertin and transcardially perfused with 50 ml of 4% paraformaldehyde in phosphate-buffered saline (PBS). Muscles were washed in PBS overnight, and spinal cords and brains were post-fixed in the 4% paraformaldehyde overnight and then all were processed for cryoprotective embedding. For visualization of the NMJ in various whole muscles, α-bungarotoxin conjugated to tetramethylrhodamine (TMR), Alexa fluor 488, or Alexa fluor 647 (Invitrogen, Carlsbad, CA, Carlsbad, CA) 1:200 was added with goat anti-VAChT 1:2000 (Sigma-Aldrich, St. Louis, MI). For analysis of motor groups in the brainstem and spinal cord, the following primary

antibodies were used: goat anti-ChAT 1:100 (Millipore, Billerica, MA), rabbit anti-MMP-9 1:4000 (Abcam, Cambridge, MA), goat anti MMP-9 1:2000 (Sigma-Aldrich, St. Louis, MI), rabbit anti-GFP 1:1000 (Invitrogen, Carlsbad, CA), chicken anti beta-galactosidase 1:2000 (Abcam), mouse anti-NeuN 1:600 (Chemicon, Billerica, MA), and rabbit anti-phosphorylated EIF2α (Ser51) 1:150 (Cell Signaling Technology, Inc. Beverly, MA). Secondary antibodies conjugated to Alexa fluor 488, 555, and 594, and 647 were generated in Donkey (Invitrogen, Carlsbad, CA). Images were acquired on a Nikon Eclipse TE-2000-E fluorescent microscope. The protocol was modified slightly for p- EIF2α staining; slides were blocked in 3% BSA, 0.3% triton X and the primary antibody remained on the slides for at least 48 hours. Staining was always performed alongside a negative control so that when imaged the exposure could be adjusted to the control levels to reduce background.

In situ hybridization

Tissue preparation was performed as described above and *in-situ* hybridization protocol was followed as previously described (Arber et al., 2000) on tissue from male P7 or P57 wild-type C57BL/6J mice (unless otherwise specified in the text). Probes were generated from cDNA vectors purchased from Open Biosystems Inc. (Huntsville, AL). These included the following OpenBiosystem (clone ID numbers are in parentheses): *Pou4f3 (*7618100*), Mmp9* (6309245), *Egln3 (*6528802*), Trhr* (40048176), *Hsd17b2* (4217153), *Nts* (5691298), *Npr3 (4019152), Cartpt (*6817832*) Mmp2 (*6813184*), Timp2 (6821553), Timp3 (4239015), Kcnj5 (*40045462*), Arghap9* (4987970), *Agtr2* (3497420), *Fbxw8* (5102839), *Il1f9* (40091521), *Gad2* (4482097), *Rpp25* (5367203). *Sema3e* cDNA was generously provided by Dr. Sophie Chauvet (Developmental Biology Institute of Marseille Luminy). *Chat* and *Kcnj14* cDNA vectors were previously generated in the Henderson laboratory. Vectors contained either full-length cDNA sequences or the sequences corresponding to the 5' UTR regions of genes of interest flanked by either SP6, T3, or T7 promoters. For each of these, clones were first linearized at the 5' end of the cDNA sequences with restriction enzymes and used as a templates for synthesis of antisense RNA probes using either T7, SP6, or T3 polymerases, depending on which of the promoters was located to the 3' of the cDNA sequence, and digoxigenin (DIG)-labeled UTPs (Roche Applied Science, Indianapolis, IN). Successful synthesis was verified by running the labeled RNA probes on 1.2 % agarose gels to check for appropriate sizes.

Retrograde labeling

Cholera toxin subunit B conjugated to Alexa Fluor 488 or 555 was injected was injected into the Sol, TA, or IC muscles of WT mice at P5 or P40 or *Mmp9*$^{-/-}$ mice at P40. Animals were perfused and spinal cords

were collected 48-96 hrs later. At that time, the injected muscle and surrounding muscles were checked for fluorescence to assure specificity of injections.

Behavioral assays

Mice were assessed for motor function using the accelerated rotarod task twice weekly from P40 onward. Briefly, we weighed each mouse before the trial and then placed animals on an accelerating rod (4-40 rpm over a 5-minute period) and recorded the time it took for each mouse to fall from the rod. We performed 2 trials at each time point for each animal and recorded the longest time taken to fall and used it in analyses. A decrease in time on the rotarod was observed with increasing motor impairment.

We also used a weekly swim tank test to assess progression of motor deficit from P40 onward. The test was constructed as per the specifications of Raoul et al. (2005) with slight modifications. Test subjects were dropped individually into one end of a 75-cm long x 6-cm wide x 40-cm high Plexiglas container filled partially with 20°C water and induced to swim to a ramp at the other end that protruded into the water. Footage of each trial was recorded using a high-speed video camera. Each subject underwent a minimum of five trials, with the shortest time excluded from analysis and the next three shortest times averaged to obtain a value for that individual and time point. Length of swim was determined from when the hindlimbs first contacted the surface of the water to their first contact with the ramp. A progressive slowing of an animal's swim rate was considered a signal of hindlimb motor dysfunction.

Electrophysiological measurements

Mice were anaesthetized with inhalational isoflurane. Two stimulating electrodes were placed on both sides of the sciatic nerve. A controlled stimulation was applied to the nerve to evoke and record unitary and maximal isometric twitch and tetanic isometric contractions from each muscle. Beginning at a stimulus voltage of 100 μs duration that was below the threshold for recruitment of motor units, we applied a manually controlled graded 0 to 10 V electrical stimuli to the sciatic nerve at a frequency of 0.5 Hz and recorded the response. The M-wave was measured at each escalating amplitude, until the maximal response was elicited and did not increase further.

Experiments with AAV6 viral vectors

Generation of AAV6 vectors:

AAV6:Mmp9: The cDNA for full-length mouse Mmp9 (Open Biosystems, Huntsville, AL) was subcloned into the AAV6 parent vector placing *Gfp* cDNA under the control of the CMV promoter.
The following sequences were subcloned into the AAV6:shSOD1 vector (Towne et al., 2008) replacing the shRNA sequence targeting mutant SOD1 with TRC31231 under the H1 promoter:
AAV6:*shMmp9 :* the TRC31231 clone, which expresses an shRNA sequence 5'GAGGCATACTTGTACCGCTAT3' targeting nt 145 – 165 in the coding region of *Mmp9*
AAV6:mismatch : an off-target shRNA control vector containing an shRNA insert that does not target any human or mouse genes (SHC002)
Both were purchased from Sigma Aldrich (St. Louis, MI). AAV6 virus was produced and concentrated as previously described (Towne et al., 2009). Viral titers for AAV6:U6-sil MMP9 (trc31) were 2.1 x 10^{14} vg/ml and AAV6:U6-mis MMP9 were 2.3 x 10^{13} vg/ml.

Vector administration: For intracerebroventricular (i.c.v) injections, P1 pups were anesthetized by hypothermia by placing them on wet tissue overlaying the ice for 2 minutes. Pups were placed ventral side down onto the metal stage that was previously cooled on ice and stabilized with scotch tape. To identify the injection site on the skull a diagonal from lambda to the eye was traced. A point 1 mm away from the midpoint toward lambda was marked. Using 31 Gauge 1/2 cc Insulin syringe (BD Ultra-Fine* II Short Needle Insulin Syringe, VWR) 2 µl of virus was injected at the marked point into the third ventricle. 3mm was the maximum depth the syringe was allowed to penetrate the skull. Virus solution was colored by addition of a small amount of Fast Green dye (Sigma-Aldrich, St. Louis, MI). Success of the i.c.v injections was monitored by transilluminating the head of the injected pup to assess whether the dye spread to both ventricles. If the dye did not spread to both ventricles, the injections were deemed unsuccessful and the pups were sacrificed. For intramuscular (i.m.) injections, P4 pups were anesthetized by hypothermia. The skin overlaying the TA muscles was opened and 1-2 µl of the AAV6.shMMP9 virus was injected using an insulin syringe. Following that injection, the pup was flipped and the contralateral TA muscle was injected with 1-2 µl of the AAV6:mismatch virus. Successfully injected pups were allowed to recover for 5 -10 min on the warming blanket before being returned to the mother. For the AAV6.MMP9 i.m. administration, P4 pups were anesthetized and then 2 µl of the viral vector was injected into their TA, soleus, or extraocular muscles. Following that injection, the pup was flipped and the contralateral TA, soleus, or extraocular muscle was injected with 2 µl of the AAV6:GFP virus.

Anatomical and Statistical analyses

For the quantification of VAChT and BTX staining of muscle cryosections, consecutive longitudinal 40 µm cryosections of muscles were stained with VAChT and BTX. Images were acquired using Nikon Eclipse TE-2000-E fluorescence microscope using 4x objective maintaining individual pixel intensities in the linear range. For large muscles (TA, Sol, IC, BC, EAS, EUS) this analysis was performed on every second section. For the extraocular muscles, every section was used. NIS-Elements 3.0 software (Nikon Instruments Inc, Melville, NY) was used to process the images. A region of interest was drawn manually around the synaptic band. For each image, pixel intensity in the region of muscle outside the synaptic band in each channel was sampled and designated as background. Binary thresholding was performed to identify discrete areas of pixel intensity above background levels. These areas were counted in both VAChT and BTX channels. Areas of overlap between the two channels were identified and counted. %NMJ innervation was determined by dividing the total number of areas of overlap between VAChT and BTX signals (total number innervated endplates) by the number of areas containing BTX signal (total number of endplates).

For the quantification of motor neuron numbers, motor neurons were counted in consecutive transverse 20 µm cryosections of the L5 and L6 levels of the spinal cord from age- and sex-matched wild-type littermate controls stained for ChAT. A 2-mm extent of the L5-S1 spinal cord (67 sections) was sampled. In each animal, the cryosection corresponding to the L6/S1 border region was identified by visual inspection of the disappearance of the DL nucleus and the prominent V nucleus. The L6 level on each side was defined as the 1-mm region rostral to the L6/S1 border section. Motor neurons in this region were counted in every consecutive 20 µm section. DL motor neurons were identified by their characteristic location at the lateral border of the ventral horn and the characteristic positions. Motor neurons located dorsally to this population were considered to be RDL motor neurons. Only cells with $ChAT^+$ cytoplasm surrounding a clearly visible nucleolus were counted. For each animal numbers of motor neurons in L5, RDL, and DL in left and right ventral horns were then summed.

For the quantification of MMP-9 fluorescence intensity, staining for MMP-9 and ChAT was performed on 20-µm cryosections of the spinal cord and 30-µm free-floating cryosections of the brainstem. The DL and RDL regions at L6 were defined in the same manner as for motor neuron counts (see above). L5 was defined as a 1-mm region rostral to DL nucleus. Counts of $MMP\text{-}9^+$ and $ChAT^+$ motor neurons were performed in every fifth section in left and right ventral horns (10 sections total per animal). Oculomotor, trochlear, and abducens nuclei were located in coronal sections of brainstems based on the

published rostrocaudal positions in adult brainstem as previously described (Ferrucci et al., 2010). Counts were performed in six sample sections from the entire rostrocaudal extent of the oculomotor nucleus spaced at 150 μm and in two and three sample sections spaced at 60 μm for trochlear and abducens nuclei, respectively. Images were acquired using Nikon Eclipse TE-2000-E fluorescence microscope with a 10x objective, maintaining individual pixel intensities in the linear range. The two levels of MMP-9 staining intensity designated as MMP-9^{hi} and MMP-9^{lo} were clearly distinguished. Only cells with $ChAT^{+}$ cytoplasm surrounding a clearly visible nucleus were counted. To quantitatively confirm manual counts of MMP-9^{hi} and MMP-9^{lo} motor neurons, ImageJ software (National Institutes of Health, Bethesda, MD) was used to process images acquired for L5 motor neurons in one wild-type animal (273 motor neurons counted). A 5-μm^2 area within the cytoplasm of each $ChAT^{+}$ motor neuron was manually picked. The summed fluorescence intensity in the MMP-9 channel for each area was then calculated. To eliminate variation between images, a background, non-$ChAT^{+}$ point was also selected and the summed intensity from this region was then subtracted from all other intensity values from that image. The data were then sorted by intensity and plotted using Excel. A best-fit trendline, determined by maximizing the R^2 value, was then added and the second derivative was taken to find the inflection points of the function. The ordinate values of the two inflection points were considered to be the bin threshold. Specifically, all cells with an intensity lower than the first inflection point were considered MMP-9neg, all cells between the two inflection points were considered MMP-9lo and all cells above the second inflection point were considered MMP-9hi. The number of cells in each category was then compared to manual counts.

For motor neuron cell size measurements, the largest cross-sectional areas were determined using NIS-Elements 3.0 software (Nikon Instruments Inc, Melville, NY) for cells with a $ChAT^{+}$ cytoplasm with a visible nucleus. All $ChAT^{+}$ MNs with a visible nucleus were imaged at 10x and outlined. Distribution histograms were constructed for each level of MMP-9 staining intensity, by grouping cell body cross-sectional areas in 100-μm^2 bins.

Tests of significance between two genotypes were conducted using an unpaired Student's t-test. A Student's t-test was also used to for the p-EIF2α and MMP-9 co-localization analysis. Specifically, the probability of cells being co-positive by chance was calculated (#MMP9 -positive MNs/ total MNs * #p-EIF2α-positive MNs/ total # MNS), and that number was compared to the observed population of co-positive cells (co-positive cells/ total # MNs) for each animal. Tests between three or more groups were

conducted using a one-way ANOVA with a Student Newman-Keuls post hoc analysis. Survival analyses were generated by Kaplan-Meier estimates with a logrank analysis. All calculations were performed using SigmaPlot software. All α-thresholds were set at 0.05 unless otherwise specified.

Supplemental References

Arber, S., Ladle, D.R., Lin, J.H., Frank, E., and Jessell, T.M. (2000). ETS gene Er81 controls the formation of functional connections between group Ia sensory afferents and motor neurons. Cell 101, 485-498.

Ferrucci, M., Spalloni, A., Bartalucci, A., Cantafora, E., Fulceri, F., Nutini, M., Longone, P., Paparelli, A., and Fornai, F. (2010). A systematic study of brainstem motor nuclei in a mouse model of ALS, the effects of lithium. Neurobiol Dis 37, 370-383.

Raoul, C., Abbas-Terki, T., Bensadoun, J.C., Guillot, S., Haase, G., Szulc, J., Henderson, C.E., and Aebischer, P. (2005). Lentiviral-mediated silencing of SOD1 through RNA interference retards disease onset and progression in a mouse model of ALS. Nat Med 11, 423-428.

Towne, C., Pertin, M., Beggah, A.T., Aebischer, P., and Decosterd, I. (2009). Recombinant adeno-associated virus serotype 6 (rAAV2/6)-mediated gene transfer to nociceptive neurons through different routes of delivery. Mol Pain 5, 52.

Towne, C., Raoul, C., Schneider, B.L., and Aebischer, P. (2008). Systemic AAV6 delivery mediating RNA interference against SOD1: neuromuscular transduction does not alter disease progression in fALS mice. Mol Ther 16, 1018-1025.